Check for updates

ADVANCED MATERIALS
www.advmat.de

Water–Salt Oligomers Enable Supersoluble Electrolytes for High-Performance Aqueous Batteries

Shengying Cai, Xingyuan Chu, Chang Liu, Haiwen Lai, Hao Chen, Yanqiu Jiang, Fan Guo, Zhikang Xu, Chunsheng Wang,* and Chao Gao**

Aqueous rechargeable batteries are highly safe, low-cost, and environmentally friendly, but restricted by low energy density. One of the most efficient solutions is to improve the concentration of the aqueous electrolytes. However, each salt is limited by its physical solubility, generally below 21–32 mol kg^{-1} (m). Here, a $ZnCl_2/ZnBr_2/Zn(OAc)_2$ aqueous electrolyte with a record super-solubility up to 75 m is reported, which breaks through the physical solubility limit. This is attributed to the formation of acetate-capped water–salt oligomers bridged by Br^-/Cl^--H and $Br^-/Cl^-/O\text{-}Zn^{2+}$ interactions. Mass spectrometry indicates that acetate anions containing nonpolarized protons prohibit the overgrowth and precipitation of ionic oligomers. The polymer-like glass transition temperature of such inorganic electrolytes is found at ≈–70 to –60 °C, without the observation of peaks for salt-crystallization and water-freezing from 40 to –80 °C. This supersoluble electrolyte enables high-performance aqueous dual-ion batteries that exhibit a reversible capacity of 605.7 mAh g^{-1}, corresponding to an energy density of 908.5 Wh kg^{-1}, with a coulombic efficiency of 98.07%. In situ X-ray diffraction and Raman technologies reveal that such high ionic concentrations of the supersoluble electrolyte enable a stage-1 intercalation of bromine into macroscopically assembled graphene cathode.

Aqueous electrolytes resolve the concerns of battery raised over safety, cost, and environmental impact.[1–3] However, their adoption has been slower due to the lack of high-energy-density electrochemical couples that has resulted from the narrow electrochemical stability window of water (1.23 V) and low capacity of cathodes.[4] An effective method to address this problem is to adjust interactions between dissociated ions and water, which have a significant influence on parameters of electrolytes, such as viscosity, solubility, chemical reactivity, and stability.[5] In contrast to classical aqueous electrolytes (molarity of 1 mol L^{-1}), water-in-salt electrolytes characterized by a high molality of 20–30 mol kg^{-1} (m) greatly improved the energy density of aqueous batteries, by extending the electrochemical stability window to 3.0 V.[6] Furthermore, a hydrate salt could dissolve another salt of similar chemical properties to form eutectic systems.[7] Thus water-in-bisalt and hydrate melt electrolytes with higher salt concentrations as well as wider electrochemical stability windows were successfully obtained, pushing the energy density of aqueous cells closer to their non-aqueous counterparts.[8,9] As water-in-(bi)salt electrolytes have approached their physical solubility limits, it is a big challenge to further increase electrolyte contents in water. Additionally, in comparison to extending the potential window, using concentrated electrolytes to increase the capacity of aqueous energy storage devices, especially which are based on non-lithium elements have rarely been exploited.

Herein, we report a supersoluble electrolyte prepared by $ZnCl_2$ (zinc chloride), $ZnBr_2$ (zinc bromide), and $Zn(OAc)_2$ (zinc acetate) that breaks through physical solubility limits by formation of acetate-capped water-salt oligomers. This strategy significantly improves salt concentrations up to 75 m, which is much higher than those of previously reported water-in-(bi)salt/hydrate melt electrolytes (21–40 m).[6,8–11] Polymer-like structures as well as characters of such inorganic electrolytes are revealed by Raman spectroscopy, nuclear magnetic resonance (NMR) spectrum, electrospray ionization mass spectrometry (ESI-MS), and differential scanning calorimetry (DSC). An aqueous lithium-free battery charged by zinc deposition and halogen conversion-intercalation was first constructed with the water–salt oligomer electrolyte, demonstrating a high reversible capacity of 605.7 mAh g^{-1} at 1 A g^{-1}, a cutoff voltage of 1.85 V, and a lifespan more than 500 cycles.

$ZnCl_2$ or $ZnBr_2$ is able to form a water-in-salt electrolyte with a maximum molality of ≈20 m (Figure S1a,b, Supporting Information). By utilizing the eutectic effect, a $ZnCl_2/ZnBr_2$ (molar ratio of 3:1) water-in-bisalt electrolyte was made and extended the concentration limit from 20 to 35 m (Figure S1c, Supporting Information). In these solutions, thermal stability of water molecules increases with salt molality due to the reconstructed hydration environments, endowing aqueous electrolytes with heat-tolerance. Therefore, a 45 m $ZnBr_{0.5}Cl_{1.5}$+1 m

---

Dr. S. Y. Cai, X. Y. Chu, C. Liu, H. W. Lai, Dr. H. Chen, Dr. Y. Q. Jiang,
Dr. F. Guo, Prof. Z. K. Xu, Prof. C. Gao
MOE Key Laboratory of Macromolecular Synthesis and Functionalization
Department of Polymer Science and Engineering
Zhejiang University
38 Zheda Road, Hangzhou 310027, China
E-mail: xuzk@zju.edu.cn; chaogao@zju.edu.cn

Prof. C. S. Wang
Department of Chemical and Biomolecular Engineering
University of Maryland
College Park, MD 20740, USA
E-mail: cswang@umd.edu

The ORCID identification number(s) for the author(s) of this article can be found under https://doi.org/10.1002/adma.202007470.

DOI: 10.1002/adma.202007470

© 2021 Wiley-VCH GmbH

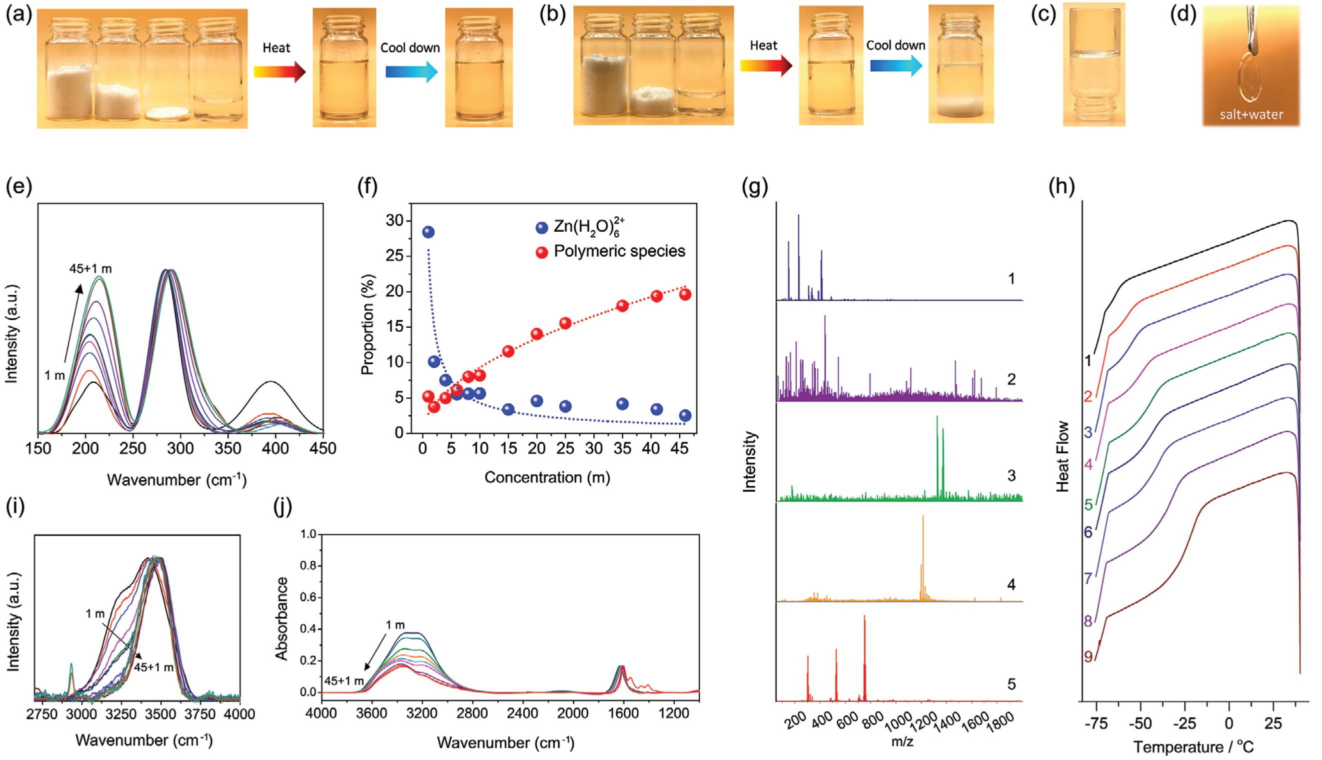

Figure 1. Electrolyte characterizations. a) WSOE$_{45}$-1 prepared by stoichiometric amounts of $ZnCl_2$, $ZnBr_2$, $Zn(OAc)_2$, and water. b) 40 m $ZnBr_{0.5}Cl_{1.5}$ suspension prepared by stoichiometric amounts of $ZnCl_2$, $ZnBr_2$, and water. c) WSOE$_{40}$-20 consisted of 20 m $ZnCl_2$, 20 m $ZnBr_2$, and 20 m $Zn(OAc)_2$. d) WSOE$_{50}$-25 consisted of 25 m $ZnCl_2$, 25 m $ZnBr_2$, and 25 m $Zn(OAc)_2$. e) Raman spectra of zinc derivatives in electrolytes, including: 1) $ZnBr_n^{2-n}$ (150, 172, 184, and 206 cm^{-1}), 2) $ZnCl_n^{2-n}$ (266, 278, 286, 305, 345 cm^{-1}), 3) polynuclear aggregate (230 cm^{-1}), and 4) $Zn(H_2O)_6^{2+}$ (390–410 cm^{-1}).[11–13] Peak differentiating analysis is shown in Figure S4, Supporting Information. f) Variation trends of $Zn(H_2O)_6^{2+}$ and polymeric species contents in 1–46 m electrolytes, obtained by the integral area of separated peaks in Figure S3, Supporting Information. g) Mass spectra of 1 m $ZnBr_{0.5}Cl_{1.5}$ aqueous solution (curve 1), 40 m $ZnBr_{0.5}Cl_{1.5}$ suspension (supernatant, curve 2), WSOE$_{45}$-1 (curve 3), WSOE$_{45}$-2 (curve 4), and WSOE$_{45}$-10 (curve 5). h) DSC results of WSOE$_{45}$-1 (curve 1), WSOE$_{45}$-2 (curve 2), WSOE$_{45}$-4 (curve 3), WSOE$_{45}$-6 (curve 4), WSOE$_{45}$-8 (curve 5), WSOE$_{45}$-10 (curve 6), WSOE$_{45}$-15 (curve 7), WSOE$_{45}$-20 (curve 8), and WSOE$_{45}$-30 (curve 9). i,j) Raman and FTIR spectra of water molecules in electrolytes. Peak differentiating analysis is shown in Figures S6–S9, Supporting Information.

$Zn(OAc)_2$ water–salt oligomer electrolyte (WSOE; WSOE$_X$-Y is used after here, where X denotes the total molality of $ZnCl_2$ and $ZnBr_2$, and Y denotes the molality of $Zn(OAc)_2$) was successfully prepared by heating stoichiometric amounts of $ZnCl_2$, $ZnBr_2$, $Zn(OAc)_2$, and ionized water at 60 °C for 2 h and then 120 °C for 72 h. As a result, a transparent and colorless liquid is obtained even at room temperature, corresponding to a high density of 2.602 g cm^{-3} (**Figure 1**a). The WSOE$_{45}$-1 is stable at 25 °C for at least 24 h as shown in Figure S2a,b, Supporting Information. Ionic conductivities of the WSOE$_{45}$-1 and 1–35 m $ZnBr_{0.5}Cl_{1.5}$ are listed in Table S1, Supporting Information. The transference number of positive charge in WSOE$_{45}$-1 was measured to be 0.343 by a Zn|WSOE$_{45}$-1|Zn symmetric cell according to Equation (S1), Supporting Information (corresponding data used for calculation are displayed in Figure S3, Supporting Information). The crucial role of $Zn(OAc)_2$ in this condition is illustrated in Figure 1b, where salt precipitation occurred in a 40 m $ZnBr_{0.5}Cl_{1.5}$ aqueous solution without the addition of $Zn(OAc)_2$ during cooling process. The salt molality of WSOE was further improved to 60–75 m by adjusting the molar ratio of zinc salts, and the electrolyte transforms from a liquid to quasi-solid or hydrogel state (Figure 1c,d).

Molecular structures of 1–35 m $ZnBr_{0.5}Cl_{1.5}$ aqueous electrolytes, WSOE$_{40}$-1, and WSOE$_{45}$-1 were investigated by spectroscopies. Figure 1e and Figure S4, Supporting Information, show Raman band assignments and corresponding analysis results for zinc derivatives. The vibration band located at about 390 cm^{-1} is assigned to zinc hydrate, which underwent an intensity weakening and blue shift from 390 to 410 cm^{-1} when the salt molality was increased from 1 to 46 m. This phenomenon is ascribed to the weakened hydrolysis and enhanced hydration of Zn^{2+} in concentrated electrolytes.[11,14] Meanwhile, the areal proportion of polymeric species at 230 cm^{-1} increases from 5.2 to 19.6% (Figure 1f), implying the formation of zinc-based oligomers in concentrated electrolytes. This is further supported by ESI-MS. For 1 m $ZnBr_{0.5}Cl_{1.5}$, peaks are observed at 200.9–464.8 m/z (Figure 1g, 1), whereas molecular ions of 40 m $ZnBr_{0.5}Cl_{1.5}$ supernatant are tested to be 208.9, 438.2, 545.3, 794.3, 957.5, 1119.9, 1471.8, 1623.3, and 1795.2 m/z (Figure 1g, 2). Oversized ionic oligomers might lead to salt precipitation, thus are invisible in the supernatant of suspension. By contrast, peaks of WSOE$_{45}$-1 are mainly observed at 1328.8 m/z (Figure 1g, 3), accompanied by negligible signals around 1400–1800 m/z. The function of $Zn(OAc)_2$ is ascribed

© 2021 Wiley-VCH GmbH

to be capping agents that prevent the overgrowth of ionic oligomers. To verify this assumption, additional $Zn(OAc)_2$ (1 and 9 m) was introduced into $WSOE_{45}$-1, resulting in continuously decreased molecular weights of ionic oligomers (Figure 1g, 4 and 5). Table S2, Supporting Information, shows calculated constitutions of $WSOE_{45}$-1. As a result, both of OAc^- and H_2O are found in these water–salt oligomers as indispensable components. In addition, Raman peaks located at 305 cm^{-1} and 206 cm^{-1} were originated from vibrations of molten $ZnCl_2$ and $ZnBr_2$.[15,16] Remarkable intensification of these peaks was observed with the increment of salt concentration (Figure S4, Supporting Information), indicating a structural transformation from traditional aqueous solution into molten salts. Thermal properties of electrolytes are characterized by differential scanning calorimetry (Figure 1h, 1). In contrast to dilute aqueous solutions (1 m $ZnCl_2$, 1 m $ZnBr_2$, and 1 m $ZnBr_{0.5}Cl_{1.5}$ in Figure S5, Supporting Information), no peaks are observed corresponding to salt-crystallization or water-freeze of $WSOE_{45}$-1 over the entire range examined (≈–80 to 40 °C). Alternatively, glass transition temperature (T_g) of $WSOE_{45}$-1 was measured at ≈–70 to –60 °C, suggesting a polymer-like amorphous character of ionic oligomer-based electrolytes. The T_g rises up with the increase of $Zn(OAc)_2$ content and electrolyte concentrations (Figure 1h, 2–9), which is consistent with the increased viscosity of electrolytes.

Association states of water molecules are further examined by O-H vibrations (Figure 1i,j), that reflect the chemical environments of hydrogen and oxygen atoms within different acceptor–donor pairs.[17–22] From 1 to 46 m, the areal proportion of coupled O-H stretch (Raman band at 3250 cm^{-1}; Figure S6, Supporting Information) significantly decreased from 53.8% to 5.9% (Figure S7, Supporting Information), indicating the elapse of water clusters by increasing salt concentrations. However, that of nearly non-H-bonded O—H stretch (Raman band at 3520 cm^{-1}; Figure S6, Supporting Information) only increased from 12.8% to 27.9% (Figure S7, Supporting Information), leaving an areal proportion of 66.2% for other states (Raman band at 3425 cm^{-1}; Figure S6, Supporting Information). We attribute this phenomenon to the formation of $Br^-/Cl^-\cdots H$ pairs in $WSOE_{45}$-1 as an alternative interaction for the $O\cdots H$ pair, that results in a frequency downshift of uncoupled O-H stretch. This interaction reconstructs the solvent framework of solution and connects halogen anions with water molecules to be the segment of water–salt oligomer. Fourier-transform infrared (FTIR) spectra confirmed that the H-bonded O-H content (absorption signals at 3205–3370 cm^{-1}; Figure S8, Supporting Information) in 1–46 m electrolytes only varied from 71.5% to 62.3% (Figure S9, Supporting Information), due to the opposite variate of $O\cdots H$ and $Br^-/Cl^-\cdots H$ pairs.

Electronic environments of water molecules in 1–46 m aqueous electrolytes are characterized by NMR. As shown in Figure S10a, Supporting Information, the ^1H signal is found to move toward lower chemical shifts (from 4.75 to 3.95 ppm) with increasing salt molality. This phenomenon is ascribed to the increment of surrounding electronic density and enhanced shielding of protons in water molecules, consistent with the formation of halogen–hydrogen bonds deduced by Raman and FTIR. Meanwhile, the ^{17}O signal is found to move toward higher chemical shifts (from 5.72 to 17.60 ppm) (Figure S10b, Supporting Information), indicating a decreased surrounding electronic density as well as weakened shielding of oxygen atoms which are resulted from the enhanced interaction between zinc cations and water molecules in water-salt oligomers. Peak broadening of both ^1H and ^{17}O signals are attributed to the insufficient relaxation time aroused by dramatically increased solution viscosity of concentrated electrolytes.[10]

The relationship between solution structure and salt molality is further revealed from molecular dynamics simulations (**Figure 2**a,b). Typical molecular configurations of the $WSOE_{45}$-1 and 5 m $ZnBr_{0.5}Cl_{1.5}$ are displayed in Figure 2c,d, respectively. For $WSOE_{45}$-1, significantly decreased $N_{O/H}$ is found in comparison to the 5 m electrolyte (Figure 2e; Figure S11a, Supporting Information), consistent with the disappearance of coupled O-H vibration verified by FTIR and Raman spectra. With salt molality increased from 5 to 46 m, hydration number of Zn^{2+} decreases from 5.51 to 1.15, and matches well with one of the oligomer structures calculated by ESI-MS results. Intensified $Cl^-/Br^-\cdots H$ and $Cl^-/Br^-/O_W\cdots Zn^{2+}$ interactions at 46 m are predicted by increased $N_{Cl/H}$, $N_{Br/H}$, $N_{Cl/Zn}$, $N_{Br/Zn}$ as well as reduced $d_{Ow\text{-}Zn}$ (from 1.935 to 1.835 Å) (Figure 2f–j and Figure S11b–f, Supporting Information) that bond electrolyte ions with water molecules to be water–salt oligomers. For $WSOE_{45}$-1, O_{ace} is observed inside the primary hydration sheath of Zn^{2+} ($d_{Oace\text{-}Zn}$ = 1.665 Å). Nonpolarized protons in acetate anions are unfavorable for the formation of $\text{-}CH_3\cdots Cl^-/Br^-$ interactions, thus avoid the overgrowth of ionic oligomers to form precipitations in $WSOE_{45}$-1. Structural scheme of dilute $ZnBr_{0.5}Cl_{1.5}$ aqueous solution, uncapped and acetate-capped WSOE are supplied in Figure S12, Supporting Information, on the basis of experimental and simulation results. Figure S13, Supporting Information, shows the thermo gravimetric analysis) of $WSOE_{45}$-1 and 5 m $ZnBr_{0.5}Cl_{1.5}$ aqueous solution. A gentler profile is observed in the former, indicating the higher stability of water molecules in water-salt oligomers.

The advantages of $WSOE_{45}$-1 are demonstrated through a dual-ion battery (DIB) which is constructed by a self-standing graphene cathode (PGA) combined with a graphene fiber fabric (GFF) in the negative side (Figures S14 and S15, Supporting Information). Electrochemical impedance spectroscopy (EIS) measurements of the DIB in different time were performed to further validate the stability of $WSOE_{45}$-1 at 25 °C before other electrochemical tests. Similar Nyquist plots were obtained at 0, 6, 12, and 24 h in the area of high frequency (Figure S16, Supporting Information), which indicate a stable state of the assembled cell (including the electrolyte) with unchanged intrinsic/charge transfer resistance (R_s and R_{ct}). Although the increased slope of Nyquist plots at low frequency was observed as time passed, it is ascribed to the wettability of electrodes by $WSOE_{45}$-1. The battery mechanism is illustrated in **Figure 3**a. Upon charging, Br^- is oxidized to a near-zero state Br^0 and the latter intercalates into the graphite lattice of PGA cathode, resulting in a $C_n[Br]$ graphite-intercalated compound (GIC).[23] This procedure corresponds to the increased current of cathodic cyclic voltammetry (CV) curves between 1.0 and 1.35 V (versus Ag/AgCl), obtained by a three-electrode system (red plot in Figure 3b). Meanwhile, the Zn/GFF anode is formed in situ by electrodeposition of Zn on GFF below -0.65 V (versus Ag/AgCl) (blue plot in Figure 3b). During discharge, Br de-intercalates

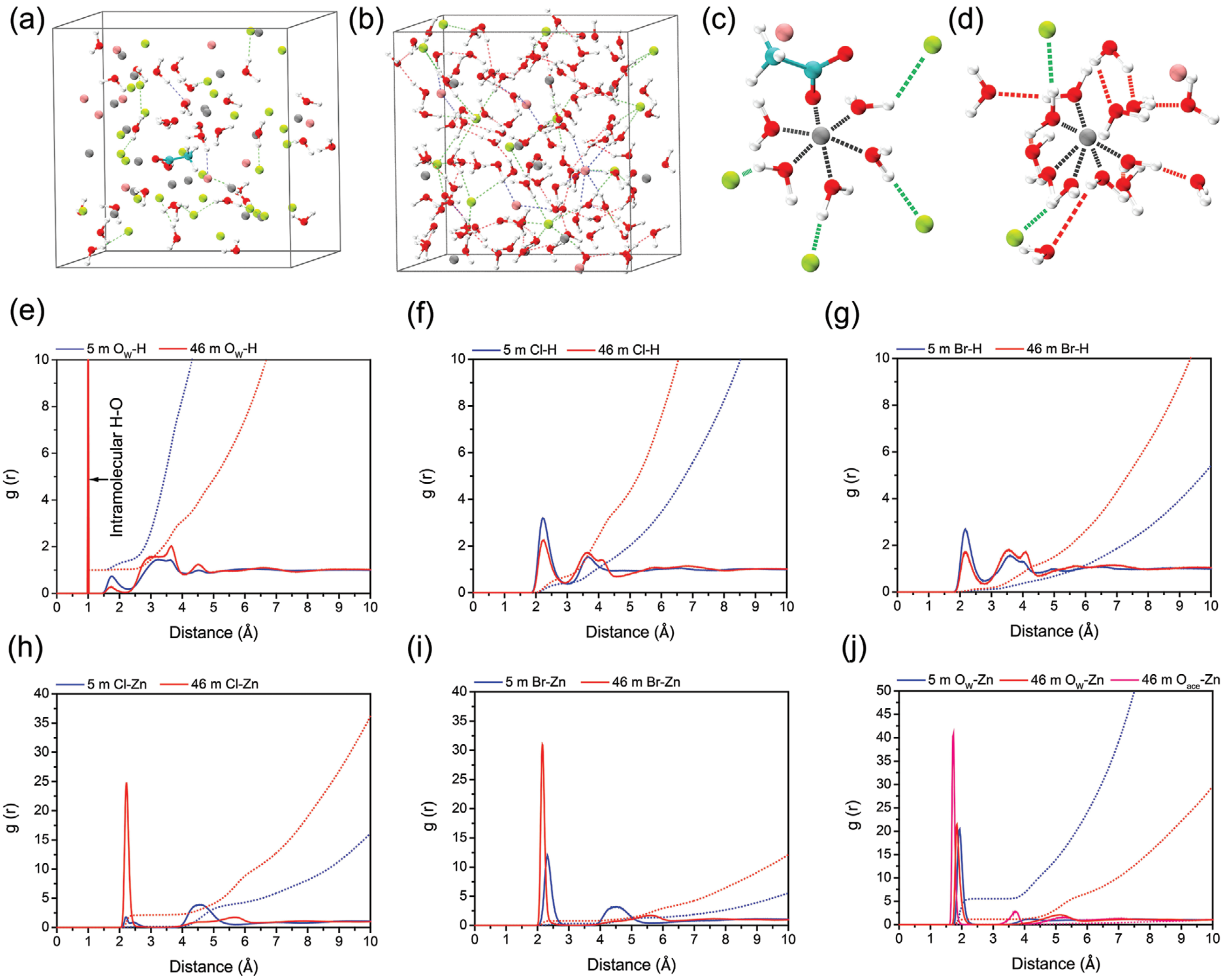

Figure 2. Molecular dynamics simulation. a,b) Snapshots of the WSOE$_{45}$-1 (a) and 5 m ZnBr$_{0.5}$Cl$_{1.5}$ aqueous solution (b) during MD simulations. Atom colors: Zn, gray; O, red; H, white; C, blue; Cl, green; Br, purple. Interactions: O···H, red line; Cl$^-$···H, green line; Br$^-$···H, blue line; O···Zn^{2+}, gray line. c,d) Typical molecular conformations extracted from patterns A and B. e–g) Radial distribution functions (solid line) and integral curves (dashed line) of H atoms, h–j) Zn atoms in 5 m ZnBr$_{0.5}$Cl$_{1.5}$ aqueous electrolytes and WSOE$_{45}$-1. Abbreviations: O$_W$ denotes oxygen atoms from water molecule, and O$_{ace}$ denotes oxygen atoms from acetate anions.

from the graphene interlayer and reduces into Br$^-$, consistent with the reduction peak of anodic CV curves under 1.0 V (versus Ag/AgCl). Simultaneously, Zn on the GFF is oxidized to Zn^{2+} again, verified by the oxidation peak that locates at –0.65 to –0.40 V (versus Ag/AgCl).

According to the Nernst equation (Equations (S2) and (S3), Supporting Information), increment of Zn^{2+} and Br$^-$ concentrations in electrolytes will result in an increased redox potential of Zn/Zn^{2+} as well as a decreased redox potential of Br$^-$/Br. Meanwhile, due to the decreased water content in electrolytes, potentials of hydrogen and oxygen evolutions move in opposite directions to that of Zn/Zn^{2+} and Br$^-$/Br, respectively. All of these variations are beneficial for avoiding water electrolysis as the process shown in Figure S17, Supporting Information. The oxidation of Br$^-$ on Ti current collector is almost irreversible as shown in Figure S18, Supporting Information, (black plot in Figure 3b), illustrating an important role of graphene host in the reversibility of cathodic reactions. In addition, CV profile of the Zn/GFF|WSOE$_{45}$-1|PGA cell is evaluated by a two-electrode system (green curve in Figure 3b) and indicates a reaction range of 1.70–1.85 V for battery charge and 1.70–1.20 V for discharge. Figure 3c,d shows the charge/discharge behaviors of DIBs when cutoff voltages were gradually increased from 1.81 to 1.85 V at 1 A g^{-1}. The specific capacity increased from 306.2 to 605.7 mAh g^{-1} (corresponding to a GIC of C$_{3.7}$Br, calculated by Equation (S4), Supporting Information) during this process (based on the cathode mass). Given both parameters of high-specific capacity and satisfactory coulombic efficiency (CE ≈97–98%) confirmed by the galvanostatic charge–discharge (GCD) technology, 1.85 V was considered as an ideal cutoff voltage for the Zn/GFF|WSOE$_{45}$-1|PGA cell. For comparison, GCD curves of DIBs beyond 1.85 V are shown in Figure S19, Supporting Information. The coulombic efficiency decreases in these

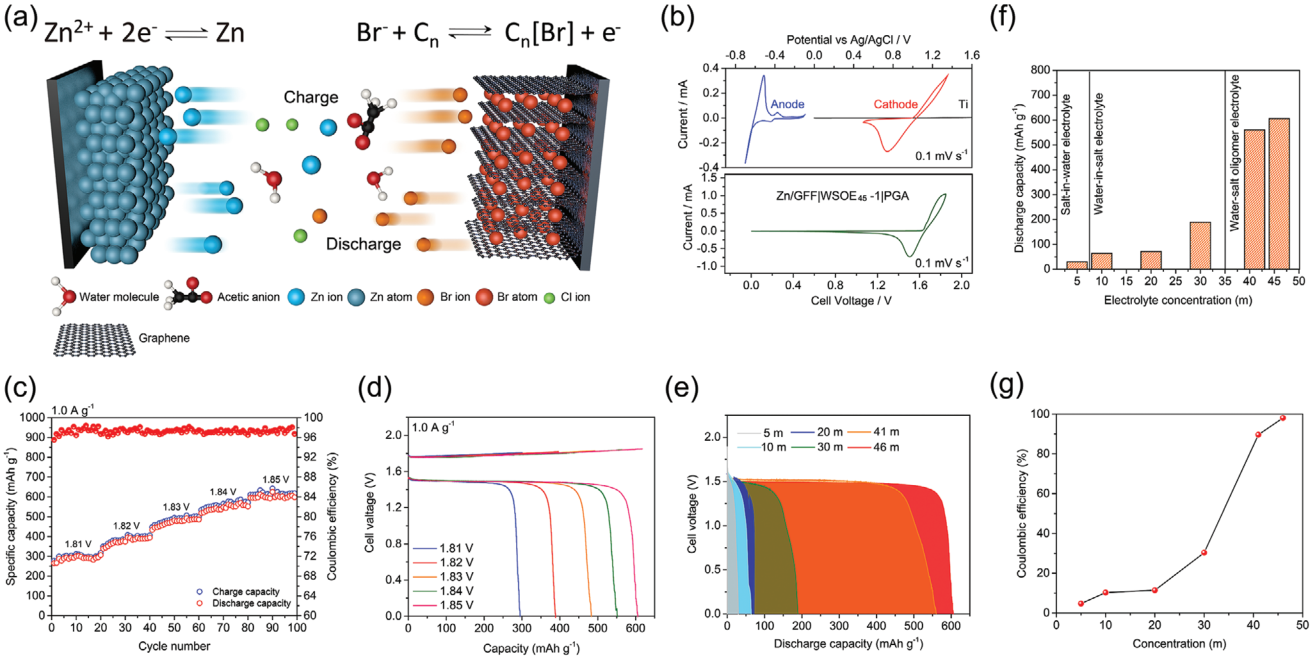

Figure 3. High-capacity aqueous dual-ion battery enabled by WSOE$_{45}$-1. a) Schematic diagram for the dual-ion battery enabled by WSOE$_{45}$-1, PGA cathode, and Zn/GFF anode. b) Cyclic voltammetry curves of anode, cathode, current collector, and dual-ion battery using the WSOE$_{45}$-1 as electrolyte. c,d) Charge and discharge capacities of the Zn/GFF|WSOE$_{45}$-1|PGA dual-ion battery at various voltages. e,f) Discharge capacity of assembled dual-ion batteries using 5–46 m electrolytes. g) Coulombic efficiency of assembled dual-ion batteries using 5–46 m electrolytes.

situations. We attribute this phenomenon to the completely saturated lattice of Br-GIC which cannot accommodate and stabilize more bromine at higher voltages.

In order to demonstrate the crucial role of supersoluble electrolyte in the reversible halogen conversion-intercalation chemistry,[23] DIBs based on 5, 10, 20, 30 m $ZnBr_{0.5}Cl_{1.5}$, WSOE$_{40}$-1, and WSOE$_{45}$-1 were fabricated. As shown in Figure 3e–g and Figure S20, Supporting Information, the discharge capacity of Zn/GFF|electrolyte|PGA cells significantly increases from 29.5 to 605.7 mAh g^{-1} upon the increment of salt concentrations from 5 to 46 m, meanwhile the coulombic efficiency increases from 4.72% to 98.07%. We ascribe this phenomenon to the suppressed shuttle effect and promoted intercalation of Br in the condition of concentrated electrolytes. Because most Br$^-$ ions are conserved as anionic halozinc complexes (such as $ZnBr_n^{2-n}$, as confirmed by the Raman spectra in Figure S4, Supporting Information) in concentrated zinc-based electrolytes, it is hard for the oxidized bromine to form polybromides (Br_3^-, Br_5^-, etc.) by coordinating Br$^-$ anions that widely exist in dilute aqueous solutions, which alleviates the shuttle effect of the polybromides. On the contrary, in dilute situations, Br or Br_2 species formed by oxidation of Br$^-$ anions during charging are inclined to dissolve in the aqueous solution rather than intercalate into the graphite lattice. Moreover, Br_2 that shuttled to the negative side will further corrode the anode, resulting in an inefficient deposition of metallic zinc.

The rate capability of DIBs was evaluated by increasing the current density from 1.0 to 2.0 A g^{-1}, and corresponding results are shown in **Figure** 4a. The rate capability of our dual-ion batteries is compromised by ionic conductivity of water–salt oligomer electrolytes (1.28 mS cm^{-1}) due to high salt concentrations. Thus, the energy density is significantly decreased when higher current densities are employed. Although higher capacity above 605.7 mAh g^{-1} was achieved at even slower rates, the reversibility of batteries decreased in this condition (such as 0.5 A g^{-1} in Figure S21a, Supporting Information). We ascribe this phenomenon to reduced-overpotentials for Br$^-$ oxidation at low current densities, by which an excess of Br is produced at original potentials. A voltage-controlled strategy was used at 0.5 A g^{-1} to limit the over-oxidation of Br$^-$ and ensure the reversibility of batteries (Figure S21b,c, Supporting Information). In other words, the specific capacity has to be controlled around 605.7 mAh g^{-1} to avoid the decrement of coulombic efficiency. The Zn/GFF|WSOE$_{45}$-1|PGA cells demonstrated excellent cycle stability (Figure 4b), with 74.5% of initial capacity retained after 500 cycles at 1 A g^{-1}. The structure of graphene cathode was well maintained after the cycling test (Figure S22a–c, Supporting Information). The stability of Zn stripping/plating in WSOE$_{45}$-1 was also affirmed by a Zn|WSOE$_{45}$-1|Zn symmetric cell as shown in Figure S22d, Supporting Information. To explore the causes of capacity recession during long-term tests, X-ray photoelectron spectroscopy (XPS) was used to characterize the cycled PGA cathode. As a result, C—Br covalent bonds (286.9 and 70.0 eV in Figures S22e and 22f, Supporting Information, respectively) were found in the cycled PGA at a discharged state,[24,25] which account for the recession of battery capacity by weakening the reversibility of Br-intercalation/deintercalation. This problem should be overcome in the future work. We measured the EIS of PGA cathode in WSOE$_{45}$-1 with a three-electrode setup at different states of charge (SOC). As a result, the interfacial resistance between PGA cathode and electrolyte ($R_{ct,1}$ in Figure 4c) decreases with SOC (from 224.7 to 211.3 Ω), which can be explained by infiltration

© 2021 Wiley-VCH GmbH

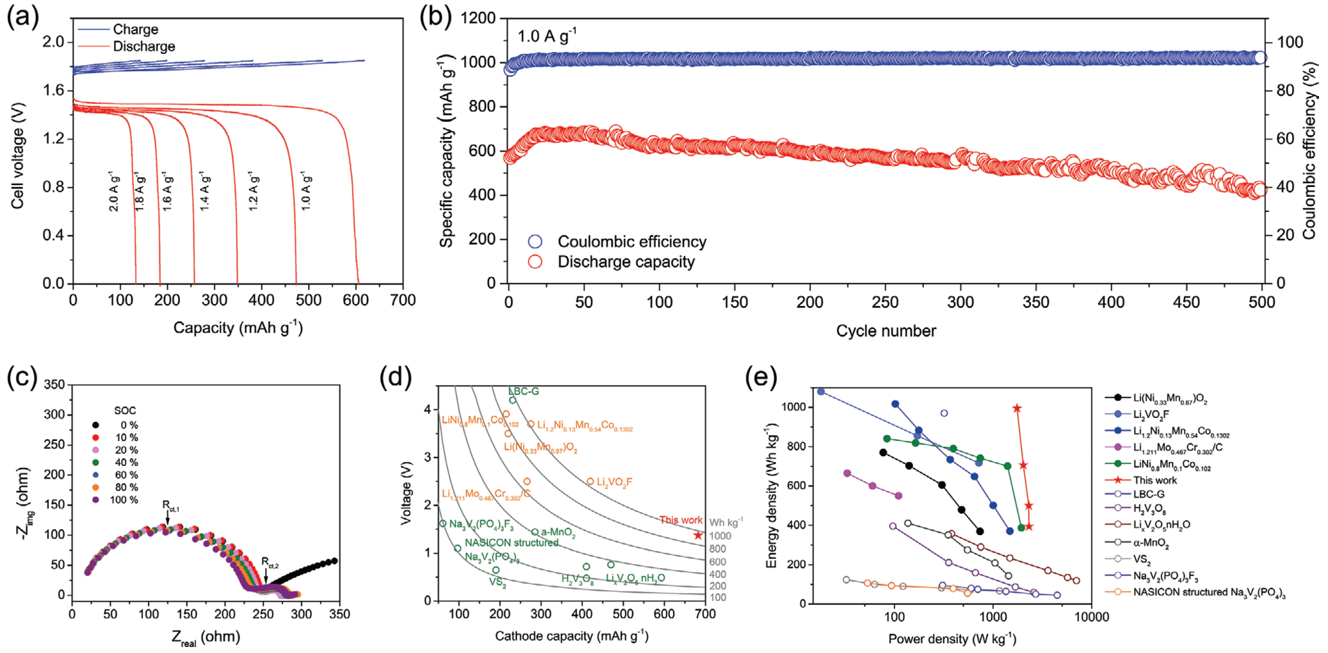

Figure 4. Electrochemical performance. a) Galvanostatic charge–discharge profiles of the dual-ion battery at various rates. b) Cycling stability of the dual-ion battery at 1 A g^{-1}. c) Nyquist plots of the PGA cathode in WSOE$_{45}$-1 at various SOCs, obtained by a three-electrode setup. The Zn foil and Ag/AgCl were used as the counter electrode and reference electrode, respectively. d) Energy density of the Br-intercalated PGA cathode compared with various state-of-the-art cathode using both non-aqueous (yellow circles) and aqueous (green circles) electrolytes. e) Ragone plots of the Br-intercalated PGA cathode compared with various non-aqueous (solid circles) and aqueous (hollow circles) cathodes. All of the above data were based on the WSOE$_{45}$-1. The anode used for NASICON-structured $Na_3V_2(PO_4)_3$, $Na_3V_2(PO_4)_3F_3$, VS_2, α-MnO$_2$, $Li_xV_2O_5{\cdot}n$H$_2$O, and $H_2V_3O_8$ in (d) and (e) is zinc metal, and that used for $LiNi_{0.8}Mn_{0.1}Co_{0.102}$, $Li_{1.211}Mo_{0.467}Cr_{0.302}/C$, $Li_{1.2}Ni_{0.13}Mn_{0.54}Co_{0.1302}$, Li_2VO_2F, and Li[Ni$_{1/3}Mn_{2/3}$]O$_2$ in (d) and (e) is lithium metal. Only the LBC-G is coupled with a graphite anode.

of the WSOE$_{45}$-1 into electrodes. Simultaneously, the intrinsic resistance of the Nyquist plot is also gradually reduced (from 22.8 to 20.1 Ω), which is caused by the increased electrical conductivity of graphene assembly after Br-intercalation.[25] During charge, a new interfacial resistance ($R_{ct,2}$ in Figure 4c) is observed and increases with SOC (from 31.3 to 51.1 Ω). This result is attributed to accumulated halogen species on the cathode. More detailed analyses of the Nyquist plots are provided in Figure S23, Supporting Information. The most significant advantage of our DIBs is the high specific capacity of PGA cathode in WSOE$_{45}$-1, which is benefited from the ultrahigh ionic concentration of electrolyte. The energy density of PGA cathode was calculated to be 908.5 Wh kg^{-1} (the theoretical cell-level energy density is 109.2 Wh kg^{-1} or 238.2 Wh L^{-1}, calculated by Equation (S5), Supporting Information), and is greater than that of most state-of-the-art cathodes as shown in Figure 4d,e.[11,26–35] The high power density of our dual-ion batteries at 1 A g^{-1} in Figure 4e is attributed to high concentrations of electrolyte ions in the electrical double-layer near electrodes, which provide enough active materials for electrode reactions and alleviate the dependence of mass transfer. Comparisons of electrochemical performances between our dual-ion batteries and more devices are provided in Tables S3–S7, Supporting Information. Moreover, the cost of the WSOE$_{45}$-1 is much cheaper than that of previously reported concentrated electrolytes as shown in Tables S8 and S9, Supporting Information. The safety and environmental tolerance of DIBs are demonstrated by Movies S1–S3 and Figure S24, Supporting Information.

In situ Raman spectroscopy (100–500 cm^{-1}) was performed to probe the intercalated Br in graphene cathode (**Figure 5**a). A characteristic peak at 242 cm^{-1} was observed and gradually intensified with the SOC, corresponding to the stretch-mode of intercalated Br$_2$ in graphite lattice. Compared with free Br$_2$ (liquid) located at 318 cm^{-1}, a frequency downshift for intercalated Br$_2$ was found resulted from the interaction with graphene layer which weakens the interatomic bonds of halogen intercalants.[36] No free Br$_2$ peak was detected during charge/discharge processes, indicating that almost all of the oxidized bromines were intercalated into the graphitic structure of PGA cathode rather than simply absorbed on the surface of electrode, which is benefited from the ultrahigh concentration of electrolyte as abovementioned. When discharge process was carried out, the intercalated-Br peak is gradually weakened and even disappeared with the SOC at 0%, demonstrating a good reversibility of the intercalation and deintercalation process of Br. The intercalation of ions, atoms, and molecules into graphitic materials has an effect on their lattice parameters as well as Raman vibrations.[37] Figure 5b shows structural evolutions of the PGA cathode during charge/discharge processes by in situ Raman spectroscopy (1500–1650 cm^{-1}). Upon charging, Br intercalated into PGA cathode, meanwhile the graphite *G* band (1580 cm^{-1}) diminishes and first shifts to 1612 cm^{-1}, corresponding to a stage-2 Br-GIC structure.[38] The peak further shifts from 1612 to 1625 cm^{-1} at 100% SOC, indicating a stage-1 Br-GIC structure of the PGA cathode in this condition. Such a stage-1 Br-GIC was only previously observed in a single-layer graphene by

© 2021 Wiley-VCH GmbH

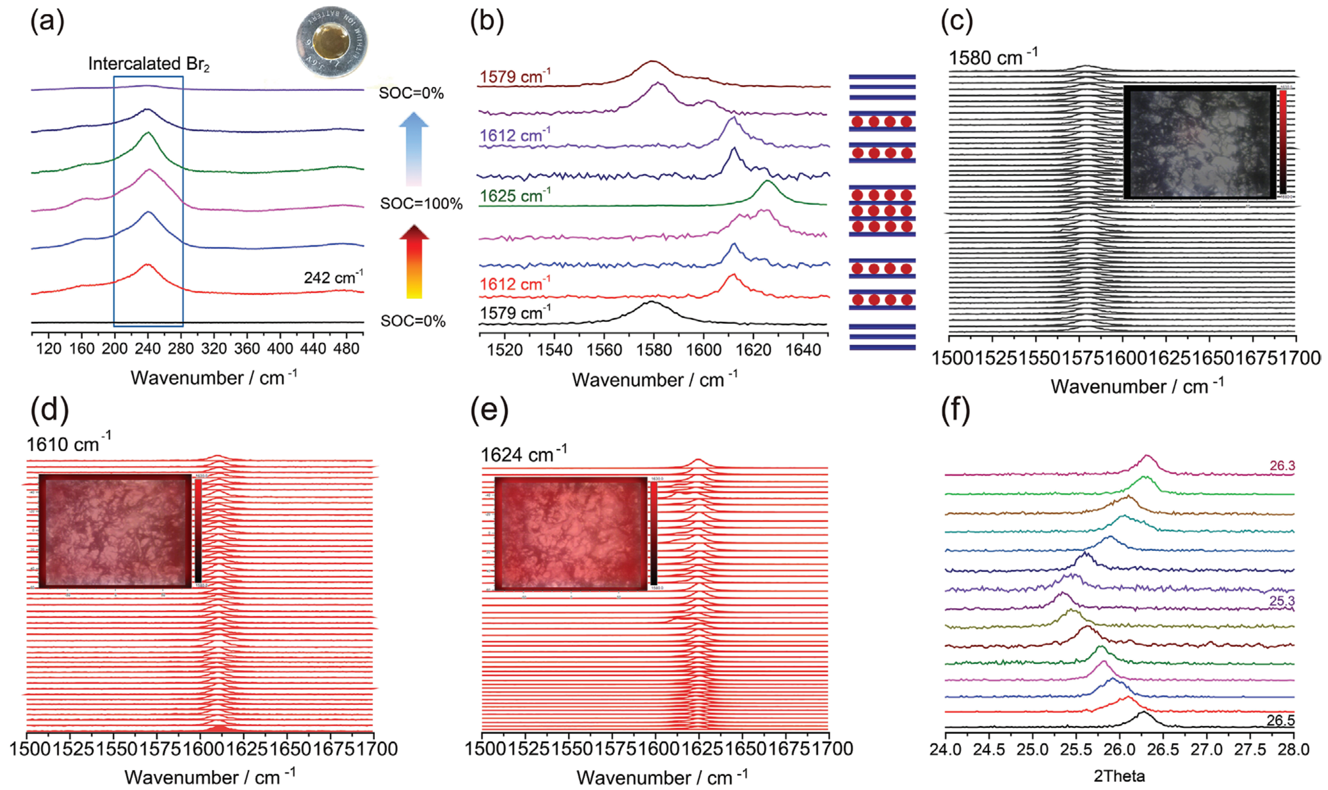

Figure 5. Energy storage mechanism. a,b) Raman spectra (100–500 cm^{-1} and 1510–1650 cm^{-1}) of Br-intercalated PGA cathode in situ during a charge–discharge cycle. c) Raman mapping and corresponding peaks of pristine PGA cathode before charge, d) stage-2 Br-intercalated PGA cathode during charge, and e) stage-1 Br-intercalated PGA cathode after charge. f) XRD profile of the Br-intercalated PGA cathode obtained in situ during a charge–discharge cycle. The color range of the maps in 5c-e refer to different Raman shift obtained on graphene cathode, and the wavenumber increases from blackness to redness.

Jung et al., whereas it is hardly to be achieved in macroscopic graphene assemblies (such as the PGA cathode) by chemical doping.[38] We attribute the stage-1 Br-GIC structure of PGA to the two reasons: 1) The activity of electrolyte (Br^-) is increased by salt molality,[39] that promotes the oxidation of Br^- anions. 2) The dissolution of oxidized Br into electrolyte is suppressed by highly concentrated WSOE$_{45}$-1 (Figure S25, Supporting Information) that promotes the intercalation of Br into graphene lattice. Reversible process was observed during discharge. In addition, Raman mapping demonstrates uniform structures of pristine (Figure 5c) and Br-intercalated PGA cathode at different stages (Figure 5d,e).

X-ray diffraction (XRD) tests were also in situ performed with a DIB cell (Figure 5f). The (002) peak of PGA cathode experienced continuous shifting from 26.5° to 25.3° during charging process, indicating the gradual expansion of graphene interlayers with Br-intercalation. The *d*-spacing of PGA cathode at 100% SOC is calculated to be 0.352 nm, which is quite close to the theoretical value (0.35 nm) of stage-1 intercalated Br-GIC.[23] Upon discharging, de-intercalation of Br occurred and the expanded graphene layer gradually recovered to its pristine state again (d_{002} = 0.338 nm), representing the recovery of graphene structure in a complete charge/discharge cycle.

In summary, the polymer-like inorganic WSOEs consisted of acetate-capped water–salt oligomers break through physical solubility limits of aqueous electrolytes and demonstrate their advanced performances for rechargeable batteries. In comparison to lithium-ion batteries (LIBs) that are troubled by limited amount and non-uniform distribution of lithium source on the earth, WSOE-based batteries driven by concentrated zinc and halogen elements provide a complement technology for low-cost and highly safe energy storages. Additionally, the WSOE may also be favored in other areas, such as polymer-free solid electrolyte and synthesis media.

Experimental Section

Materials: Zinc chloride (≥98.0%), zinc bromide (≥99.9%), and zinc acetate (≥99.0%) were purchased from Shanghai Aladdin Bio-Chem Technology Co., Ltd. Graphene oxide with average lateral size of 20 µm was acquired from GaoxiTech Co., Ltd. All reagents were used as received without any further treatment. Deionized water was generated by PW Ultrapure Water System and had a resistivity of 18 MΩ cm.

Preparation of Electrolyte: WSOE: Typically, the WSOE$_{45}$-1 was prepared by dissolving 9.200 g (0.0225 mol) $ZnCl_2$, 5.067 g (0.0675 mol) $ZnBr_2$, and 0.367 (0.002 mol) $Zn(CH_3COO)_2$ in 2.0 g deionized water, and then heated at 60 °C for 2 h and then 120 °C for 72 h. Resultant solutions were cooled at room temperature before tests. Conventional electrolytes: 1–30 m $ZnCl_2$, 1–30 m $ZnBr_2$, and 1–35 m $ZnBr_{0.5}Cl_{1.5}$ aqueous solutions were prepared by dissolving zinc salts in water solvent at 60 °C under stirring, and cooled down at room temperature before tests.

NMR: NMR spectra were obtained on a Brulcer 500 MHz NMR spectrometer (DMX-500). Typically, 0.5 mL of electrolyte was added into a 5 mm glass NMR tube for characterization and chloroform-d ($CDCl_3$) in a sealed coaxial glass tube was used for reference. NMR

© 2021 Wiley-VCH GmbH

tubes were immediately sealed with plastic septa wrapped with parafilm to limit exposure to atmospheric moisture. Data were processed in MestReNova 11.0.4.

Raman Spectroscopy for Electrolytes: Electrolyte was dropped in a dry glass slide and then immediately tested by inVia-Reflex (Renishaw plc) with a laser of 532 nm wavelength.

Electrospray Ionization Mass Spectrometry: The electrolytes were first diluted by anhydrous methyl alcohol (mass ratio = 1:50), and then used for analysis.

FTIR Spectroscopy: FTIR spectra were collected by a Nicolet 5700 spectrometer, mounted with an attenuated total reflectance accessory. Electrolyte solutions were analyzed using 16 scans with a 4 cm^{-1} resolution from 4000 to 650 cm^{-1}. Background correction was performed by measuring the ambient atmosphere in the same conditions.

DSC: DSC traces were obtained on a Perkin Elmer DSC4000. Electrolytes (≈5–10 mg) were added into aluminum Tzero pans and hermetically sealed with a Tzero Sample press. Samples were cooled from room temperature to −80 °C at a rate of 5 °C min^{-1}.

MD Simulations: The simulation box consisted of a cube box with length of 50 Å containing several ion pairs and water molecules. Parameters of the atomistic models of OAc were based on the OPLS-AA force field.[40] The parameters of Zn^{2+} ion are shown in Table S10, Supporting Information. For water molecules, the four-site water model TIP4P/Ew was used.[41] 3D periodic boundary conditions were used to avoid the influence of the box boundary during simulations. The cut-off distance of non-bonded interactions was 13 Å and the long-range electrostatic interactions were calculated by the particle-mesh Ewald method.[42] Initial structures for molecular dynamic simulation were constructed by Packmol software package.[43] The ion pairs of salts and water molecules were randomly placed in a simulated box for providing homogeneous structures. Prior to the dynamics simulation, the steepest descent algorithm was used to pre-equalize the system for eliminating the excessive stress in initial structures.[44] After pre-equilibrium, an *NPT* ensemble was used to equilibrate the system under room conditions (298 K and 1 atm) for 10 ns which can converge the density of the system to a stable value. Then, 35 ns production simulation in the *NVT* ensemble at 298.15 K was carried out for data collection. The density and potential energy changes of the $WSOE_{45}$-1 system during the *NPT* process are shown in Figure S26a,b, Supporting Information. The mean square displacement of each species from 0 to 30 ns in the *NVT* process is shown in Figure S26c, Supporting Information. Both *NPT* and *NVT* simulations used time step of 1 fs. Temperature and pressure coupling were performed using v-rescale thermostat and Berendsen barostat.[45,46] All simulations were carried out by using the GROMACS 2018.6 software package.[47] All visualization structures are provided by VMD 1.9.3 software. Radial distribution functions (RDF) $g(r)_{A-B}$ was calculated by:

$$g(r)_{A-B} = \frac{1}{\rho_B}\frac{1}{N_A}\sum_{i=1}^{N_A}\sum_{j=1}^{N_B}\frac{\delta(r_{ij}-r)}{4\pi r^2} \tag{1}$$

with ρ_B the particle density of type B averaged over all spheres around particles A.

The coordination number is determined by the number of particles in the first solvation shell of the ion. Therefore, the integral value of the radial distribution function at the first valley is the coordination number. The corresponding integral number is calculated by the following equation:

$$N(r) = 4\pi\rho_N\int_0^r r^2 g(r)\,dr \tag{2}$$

where ρ_N is the average number density of coordination atoms. This method has been reported in the literature.[48–50] The corresponding valley used for calculating coordination numbers are provided in Table S11, Supporting Information.

Preparation of the Electrode: PGA cathode was obtained by previously reported method.[51] First, graphene oxide (GO) solution (5 mg mL^{-1}) was freeze-dried to get GO aerogel. It was then reduced by hydrazine hydrate at 95 °C and carbonized at 3000 °C for 1 h in a graphite furnace which was under the protection of argon flow to remove oxygen-containing groups and restore defects. The resulted aerogel was finally compressed into porous papers to get the PGA cathode. Zn/GFF anode was formed by in situ deposition of Zn on graphene fiber non-woven fabrics,[52] which was prepared by filtration of GO fibers in a mixture of water and ethanol (volume ratio of 3:1), followed by chemical reduction and high temperature carbonized at 3000 °C.

Electrochemical Measurements: In the three-electrode cells, the PGA cathode (Zn/GFF anode or Ti current collector) was used as the working electrode, Zn foil as the counter-electrode, and Ag/AgCl as the reference electrode. Cyclic voltammetry tests were carried out by a CHI 660E electrochemical work station. The EIS measurement was performed on the Multi Autolab M204 (Metrohm) using a 5-mV perturbation with frequency in the range of 0.01–1 000 000 Hz at room temperature. The dual-ion batteries were assembled as CR2025-type coin cells using PGA as the cathode (areal loadings were ≈2.79 mg cm^{-2}) and Zn/GFF as the anode. A titanium metal foil disk was placed between the cathode and the coin cell case to prevent corrosion. Glass microfiber filters (thickness of 435 µm; Whatman 934-AH) were used as the separator. After assembly, the electrochemical performances were evaluated by CHI 660E and Multi Autolab M204. The galvanostatic cycling measurements at 25 °C (in a constant temperature humidity chamber) were carried out on a Land BT2000 battery test system. The Zn|$WSOE_{45}$-1|Zn symmetric cell was assembled and tested in a similar way. Soft pack cells were fabricated with the PGA cathode, Zn/GFF anode, $WSOE_{45}$-1, titanium foil current collector (for cathode), and glass fiber filters.

In Situ Raman Spectroscopy for PGA Cathode: For the in situ Raman measurements, a Zn/GFF|$WSOE_{45}$-1|PGA cell with a kapton optical window on the cathode side was charged and discharged at 1 A g^{-1}. Raman spectra and mapping patterns were directly collected on the in Via-Reflex (Renishaw plc) using a laser of 532 nm wavelength.

In Situ XRD Study of PGA Cathodes: For the in situ XRD measurements, a Zn/GFF|$WSOE_{45}$-1|PGA cell with a Kapton window on the cathode side was charged and discharged at 1 A g^{-1}. During this process, the battery was directly put on the X-ray diffractometer to obtain immediate results. The *d*-spacing of PGA cathodes could be calculated from the diffraction angles by Bragg's law.

Supporting Information

Supporting Information is available from the Wiley Online Library or from the author.

Acknowledgements

S.C. and X.C. contributed equally to this work. This work was supported by the National Natural Science Foundation of China (Nos. 51533008, 51603183, 51703194, and 21805242), the National Key R&D Program of China (No. 2016YFA0200200), the Hundred Talents Program of Zhejiang University (188020*194231701/113), the Key Research and Development Plan of Zhejiang Province (2018C01049), and the Fundamental Research Funds for the Central Universities (Nos. 2017QNA4036 and 2017XZZX001-04).

Conflict of Interest

The authors declare no conflict of interest.

Keywords

aqueous rechargeable batteries, supersoluble electrolytes, water–salt oligomers, zinc–halogen chemistry

Received: November 1, 2020
Revised: December 10, 2020
Published online:

[1] H. Kim, J. Hong, K. Y. Park, H. Kim, S. W. Kim, K. Kang, *Chem. Rev.* **2014**, *114*, 11788.
[2] W. Li, J. R. Dahn, D. S. Wainwright, *Science* **1994**, *264*, 1115.
[3] Y. Wang, J. Yi, Y. Xia, *Adv. Energy Mater.* **2012**, *2*, 830.
[4] F. Beck, P. Rüetschi, *Electrochim. Acta* **2000**, *45*, 15.
[5] O. Borodin, J. Self, K. A. Persson, C. S. Wang, K. Xu, *Joule* **2020**, *4*, 69.
[6] L. M. Suo, O. Borodin, T. Gao, M. Olguin, J. Ho, X. L. Fan, C. Luo, C. S. Wang, K. Xu, *Science* **2015**, *350*, 938.
[7] C. A. Angell, *J. Electrochem. Soc.* **1965**, *112*, 1224.
[8] L. M. Suo, O. Borodin, W. Sun, X. L. Fan, C. Y. Yang, F. Wang, T. Gao, Z. H. Ma, M. Schroeder, A. V. Cresce, S. M. Russell, M. Armand, A. Angell, K. Xu, C. S. Wang, *Angew. Chem., Int. Ed.* **2016**, *128*, 7252.
[9] Y. Yamada, K. Usui, K. Sodeyama, S. Ko, Y. Tateyama, A. Yamada, *Nat. Energy* **2016**, *1*, 16129.
[10] M. R. Lukatskaya, J. I. Feldblyum, D. G. Mackanic, F. Lissel, D. Michels, Y. Cui, Z. N. Bao, *Energy Environ. Sci.* **2018**, *11*, 2876.
[11] C. Zhang, J. Holoubek, X. Y. Wu, A. Daniyar, L. D. Zhu, C. Chen, D. P. Leonard, I. A. Rodríguez-Pérez, J. X. Jiang, C. Fang, X. L. Ji, *Chem. Commun.* **2018**, *54*, 14097.
[12] R. B. Ellis, *J. Electrochem. Soc.* **1966**, *113*, 485.
[13] H. Kanno, J. Hiraishi, *J. Raman Spectrosc.* **1980**, *9*, 85.
[14] F. Wang, O. Borodin, T. Gao, X. L. Fan, W. Sun, F. D. Han, A. Faraone, J. A. Dura, K. Xu, C. S. Wang, *Nature Mater.* **2018**, *17*, 543.
[15] D. E. Irish, T. F. Young, *J. Chem. Phys.* **1965**, *43*, 1765.
[16] K. Fukushima, H. Yokota, H. Ibaraki, T. Nakazawa, K. Noda, Y. Iwadate, *J. Alloys Compd.* **1998**, *266*, 145.
[17] B. M. Auer, J. L. Skinner, *J. Chem. Phys.* **2008**, *128*, 224511.
[18] L. M. Uriarte, J. Dubessy, P. Boulet, V. G. Baonza, I. Bihannic, P. Robert, *J. Raman Spectrosc.* **2015**, *46*, 822.
[19] Y.-H. Zhang, C. K. Chan, *J. Phys. Chem. A* **2003**, *107*, 5956.
[20] G. E. Walrafen, *J. Chem. Phys.* **1964**, *40*, 3249.
[21] M. H. Brooker, G. Hancock, B. C. Rice, J. Shapter, **1989**, *20*, 683.
[22] B. Auer, R. Kumar, J. R. Schmidt, J. L. Skinner, *P. Natl. Acad. Sci. U. S. A.* **2007**, *104*, 14215.
[23] C. Y. Yang, J. Chen, X. Ji, T. P. Pollard, X. J. Lü, C. J. Sun, S. Hou, Q. Liu, C. M. Liu, T. T. Qing, Y. Q. Wang, O. Borodin, Y. Ren, K. Xu, C. S. Wang, *Nature* **2019**, *569*, 245.
[24] L. G. Bulusheva, V. A. Tur, E. O. Fedorovskaya, I. P. Asanov, D. Pontiroli, M. Riccò, A. V. Okotrub, *Carbon* **2014**, *78*, 137.
[25] Y. J. Liu, Z. Xu, J. M. Zhan, P. G. Li, C. Gao, *Adv. Mater.* **2016**, *28*, 7941.
[26] P. K. Nayak, J. Grinblat, M. D. Levi, O. Haik, E. Levi, M. Talianker, B. Markovsky, Y. K. Sun, D. Aurbach, *Chem. Mater.* **2015**, *27*, 2600.
[27] R. Y. Chen, S. H. Ren, M. Knapp, D. Wang, R. Witter, M. Fichtner, H. Hahn, *Adv. Energy Mater.* **2015**, *5*, 1401814.
[28] P. K. Nayak, T. R. Penki, B. Markovsky, D. Aurbach, *ACS Energy Lett.* **2017**, *2*, 544.
[29] J. Lee, A. Urban, X. Li, D. Su, G. Hautier, G. Ceder, *Science* **2014**, *343*, 519.
[30] X. L. Fan, L. Chen, O. Borodin, X. Ji, J. Chen, S. Y. Hou, T. Deng, J. Zheng, C. Y. Yang, S. C. Liou, K. Amine, K. Xu, C. S. Wang, *Nat. Nanotechnol.* **2018**, *13*, 715.
[31] P. He, Y. Quan, X. Xu, M. Yan, W. Yang, Q. An, L. He, L. Mai, *Small* **2017**, *13*, 1702551.
[32] Y. Q. Yang, Y. Tang, G. Z. Fang, L. T. Shan, J. S. Guo, W. Y. Zhang, C. Wang, L. B. Wang, J. Zhou, S. Q. Liang, *Energy Environ. Sci.* **2018**, *11*, 3157.
[33] B. Wu, G. B. Zhang, M. Y. Yan, T. F. Xiong, P. He, L. He, X. Xu, L. Q. Mai, *Small* **2018**, *14*, 1703850.
[34] P. He, M. Y. Yan, G. B. Zhang, R. M. Sun, L. N. Chen, Q. Y. An, L. Q. Mai, *Adv. Energy Mater.* **2017**, *7*, 1601920.
[35] W. Li, K. L. Wang, S. J. Cheng, K. Jiang, *Energy Storage Mater.* **2018**, *15*, 14.
[36] A. Erbil, G. Dresselhaus, M. S. Dresselhaus, *Phys. Rev. B* **1982**, *25*, 5451.
[37] D. Zhan, L. Sun, Z. H. Ni, L. Liu, X. F. Fan, Y. Y. Wang, T. Yu, Y, M. L. , W. Huang, Z. X. Shen, *Adv. Funct. Mater.* **2010**, *20*, 3504.
[38] N. Jung, N. Kim, S. Jockusch, N. J. Turro, P. Kim, L. Brus, *Nano Lett.* **2009**, *9*, 4133.
[39] M. R. Ally, J. Braunstein, *Fluid Phase Equilibr.* **1996**, *120*, 131.
[40] W. L. Jorgensen, D. S. Maxwell, J. Tirado-Rives, *J. Am. Chem. Soc.* **1996**, *118*, 11225.
[41] H. W. Horn, W. C. Swope, J. W. Pitera, J. D. Madura, T. J. Dick, G. L. Hura, T. Head-Gordon, *J. Chem. Phys.* **2004**, *120*, 9665.
[42] L. Martínez, R. Andrade, E. G. Birgin, J. M. Martínez, *J. Comput. Chem.* **2009**, *30*, 2157.
[43] M. C. Payne, M. P. Teter, D. C. Allan, T. A. Arias, J. D. Joannopoulos, *Rev. Mod. Phys.* **1992**, *64*, 1045.
[44] G. Bussi, D. Donadio, M. Parrinello, *J. Chem. Phys.* **2007**, *126*, 014101.
[45] H. J. C. Berendsen, J. P. M. Postma, W. F. van Gunsteren, A. DiNola, J. R. Haak, *J. Chem. Phys.* **1984**, *81*, 3684.
[46] M. J. Abraham, T. Murtola, R. Schulz, S. Páll, J. C. Smith, B. Hess, E. Lindahl, *SoftwareX* **2015**, *1–2*, 19.
[47] W. Humphrey, A. Dalke, K. Schulten, *J. Mol. Graph.* **1996**, *14*, 33.
[48] Y. Liu, H. G. Lu, Y. B. Wu, T. P. Hu, Q. L. Li, *J. Chem. Phys.* **2010**, *132*, 1157.
[49] R. M. D. Souza, L. J. A. D. Siqueira, M. Karttunen, L. G. Dias, *J. Chem. Inf. Model.* **2019**, *60*, 485.
[50] M. Q. Fatmi, T. S. Hofer, B. M. Rode, *J. Chem. Phys.* **2010**, *12*, 9713.
[51] H. Chen, F. Guo, Y. J. Liu, T. Q. Huang, B. N. Zheng, N. Ananth, Z. Xu, W. W. Gao, C. Gao, *Adv. Mater.* **2017**, *29*, 1605958.
[52] Z. Li, Z. Xu, Y. J. Liu, R. Wang, C. Gao, *Nat. Commun.* **2016**, *7*, 13684.